EDGE ARTICLE

Check for updates

Interface reconstruction strategy enabling the efficient light-driven amination of furfuryl alcohol

Yaorong He,[a] Xiao Wang,[a] Shanshan Ou,[a] Lin Zhu,[a] Tong Su,[a] Rongfang Zhang,[c] Wei Zhao,[a] Hui Huang,[a] Zhiqiang Wang,[a] Peiyao Du [ID] *[ab] and Xiaoquan Lu [ID] *[c]

The solar-driven photocatalytic synthesis of furfurylamine, a crucial pharmaceutical and agrochemical precursor, from renewable furfuryl alcohol, represents an energetically sustainable alternative to conventional thermal processes. Despite its promise, direct photocatalytic amination remains largely unexplored, with the current photocatalytic study predominantly focused on oxidation/reduction pathways rather than C−N bond formation. Furthermore, the deployment of biomass photoreforming is severely constrained by insufficient reaction kinetics and unsatisfactory catalytic selectivity. In this study, we present a novel reconstruction strategy to endow the catalyst with abundant active sites and greatly accelerate interfacial charge transfer. The resulting CdS/CoAl(OH)$_x$-R catalyst achieves an exceptional furfuryl alcohol conversion rate of 76.32% with 94.78% selectivity toward furfurylamine under mild conditions. This work not only provides a practical solution for sustainable furfurylamine synthesis but also offers fundamental insights into interfacial engineering for photocatalytic C−N bond formation.

Introduction

As global attention towards sustainable societies grows, artificial photosynthesis stands as one of the most feasible and promising avenues for achieving carbon neutrality.[1,2] Although solar-driven overall water splitting for hydrogen production has attracted significant research attention, this process often encounters several significant challenges, including unfavorable thermodynamics, sluggish kinetics, and rapid reverse reactions.[3,4] Sacrificial agents can partially alleviate these issues, however, their use often leads to the wasteful consumption of photogenerated holes and the generation of low-value byproducts.[5,6] In this regard, an alternative and sustainable strategy that involves coupling photocatalytic hydrogen evolution with the oxidation of biomass-derived molecules into high-value chemicals presents a win–win scenario for maximizing the utility of both electrons and holes, establishing a synergistic and economically favorable process.[7]

Furfurylamine serves as a key precursor of N-heterocyclic compounds, extensively applied in synthesizing pharmaceuticals, agrochemicals, and functional materials.[8] The conventional synthesis of furfurylamine typically relies on the energy-intensive catalytic hydrogenation of furfural, yet this process suffers from several drawbacks, including the need for costly reducing reagents,[9,10] expensive equipment requirements, multiple side reactions due to the high reactivity of furfural, and the inevitable catalyst deactivation under corrosive reaction conditions. Furfuryl alcohol is a C_5 molecule derived from the tandem hydrolysis–dehydration of hemicellulose.[11] Using more stable furfuryl alcohol instead of furfural as the raw material not only facilitates the control of side reactions but also avoids the stoichiometric consumption of reducing agents. We believe that combining photocatalytic hydrogen production with the amination of furfuryl alcohol will provide a highly attractive alternative for optimizing overall energy utilization and furfurylamine production.[12] However, to date, relevant research remains in its infancy, and to the best of our knowledge, the efficient conversion of furfuryl alcohol to furfurylamine in aqueous conditions using non-precious metal photocatalytic systems has been scarcely explored.

CdS, as a classic semiconductor photocatalyst, has garnered significant interest in solar-driven catalytic conversions due to its suitable band alignment and excellent light-harvesting properties.[13,14] However, severe photocorrosion and rapid recombination of photogenerated electron–hole pairs also hamper the performance of CdS. In view of this, strategic deposition of cocatalysts has emerged as one of the most prominent methods to improve the activity and stability of photocatalysts.[15] Among various cocatalysts, transition metal hydroxides (TMHs) are promising candidates due to their earth abundance, tunable composition, and facile synthesis.[9] However, the performance of such hybrid systems is often

[a]College of Chemistry & Pharmacy, Northwest A&F University, Yangling, Shaanxi, 712100, P. R. China. E-mail: peiyao.du@nwafu.edu.cn

[b]State Key Laboratory of Fluorine & Nitrogen Chemicals, School of Chemical Engineering and Technology, Xi'an Jiaotong University, Xi'an, Shaanxi, 710049, P. R. China. E-mail: peiyao@xjtu.edu.cn

[c]Key Laboratory of Bioelectrochemistry & Environmental Analysis of Gansu Province, College of Chemistry & Chemical Engineering, Northwest Normal University, Lanzhou, Gansu, 730070, P. R. China. E-mail: luxq@nwnu.edu.cn

compromised by the poor electrical conductivity and two-dimensional sheet-like morphology of TMHs, which limit active site exposure and efficient charge transport.[16–18] Moreover, the weak interfacial contact between CdS and TMHs can form an electronic "barrier" that impedes directional charge flow,[16] leading to suboptimal photocatalytic efficiency. Fortunately, the construction of charge transport tunnels can improve the electron–hole separation in semiconductors and charge transfer to catalysts. For instance, Bai *et al.* introduced a Au nanoparticle mediator in the core–shell ZnCdS/NiCo-LDH structure, which served as a charge transmission channel to accelerate the interface charge transfer.[19] However, the introduction of new interfaces typically creates additional defect states, which instead become electron–hole recombination sites. Therefore, rational optimization of the CdS/TMHs interface seems necessary. Beyond enhancing the intrinsic activity of photocatalytic systems and strengthened interface interactions, it is also critical to engineer rational structures that ensure full exposure of active sites, suppress photo-induced carrier recombination, and facilitate rapid mass transfer/diffusion of reactants.

Considering these factors, alkaline etching of bimetallic hydroxide precursors (*e.g.*, CoAl-TMHs) into monometallic (oxy) hydroxides within CdS/TMHs may be a prospective strategy, one that outperforms direct synthesis approaches through its unique synergistic mechanisms. First, selective dissolution during etching can generate unsaturated metal sites, significantly enhancing substrate adsorption and activation. Meanwhile, the etching-induced reconstructed interface establishes a robust built-in electric field, enabling efficient charge separation and directional migration. Additionally, strong interfacial anchoring formed through etching effectively inhibits metal leaching and improves structural stability. And, the resulting porous architecture facilitates enhanced mass transfer and diffusion, thereby accelerating reaction kinetics.

Herein, an alkaline etching engineering was proposed to reconstruct the CoAl catalyst, resulting in the formation of a CdS/CoAl(OH)$_x$-R with a deficient structure. Mechanistic investigations *via* scanning photoelectrochemical microscopy (SPECM) and intensity-modulated photocurrent spectroscopy (IMPS) confirm that the reconstructed catalyst exhibits tight interfacial interactions, enabling efficient charge transfer. In an aqueous system, CdS/CoAl(OH)$_x$-R demonstrated high activity, selectivity, and stability over at least five cycles for the photocatalytic conversion of furfuryl alcohol to furfurylamine. This work not only presents a facile and effective approach for designing high-performance photocatalysts but also advances biomass valorization into value-added chemicals to meet the goals of sustainable development.

Results and discussion

The reconstructed CdS/CoAl(OH)$_x$ catalyst was synthesized *via* a two-step process, which involved coupling CdS with CoAl(OH)$_x$, followed by alkali etching (Fig. 1a). Initially, CdS/CoAl(OH)$_x$ was prepared using a solvothermal treatment in ethylene glycol. The as-prepared CdS/CoAl(OH)$_x$ was then
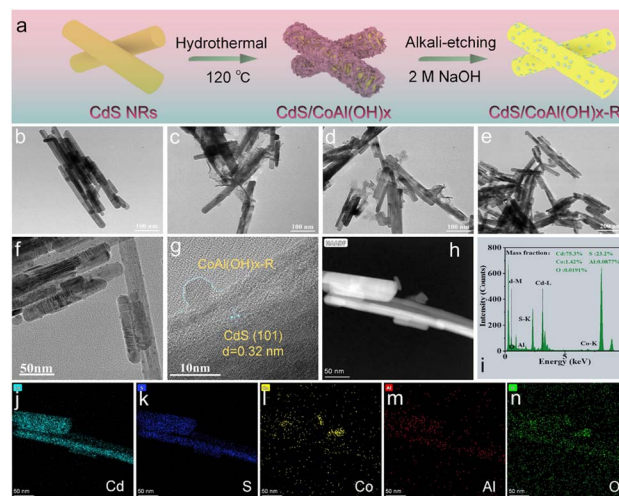

Fig. 1 (a) Schematic diagram of the preparation process, TEM image of (b) CdS, (c) CdS/Co(OH)$_x$, (d) CdS/CoAl(OH)$_x$, and (e and f) CdS/CoAl(OH)$_x$-R, (g) HR-TEM images of CdS/CoAl(OH)$_x$-R and (h–n) the corresponding elemental mapping.

subjected to thermal treatment in an aqueous sodium hydroxide solution to yield the reconstructed CdS/CoAl(OH)$_x$ (named CdS/CoAl(OH)$_x$-R).

Transmission electron microscopy (TEM) reveals the changes in the microscopic morphology of CdS/CoAl(OH)$_x$ before and after reconstruction. Following the solvothermal reaction, a thin nanosheet structure was observed to cover the surface of the CdS nanorods (Fig. 1b), forming a CdS/CoAl(OH)$_x$ composite (Fig. 1d). To elucidate the role of the Al element in shaping the morphology of the catalyst, a control sample of CdS/Co(OH)$_x$ was prepared under the same conditions. As depicted in Fig. 1c, Co(OH)$_x$ displays a dispersed thin nanosheet structure, closely resembling that of CoAl(OH)$_x$. However, following etching with a sodium hydroxide solution, the nanosheet structure on the surface of CdS was transformed into smaller nanoparticles (Fig. 1e and f), which were closely attached to the surface of the CdS nanorods. As the etching time increases, the proportion of loaded nanosheets gradually decreases, while the number of nanoparticles correspondingly increases (Fig. S1). The morphological transformation was ascribed to the thermodynamic instability of the defect structures formed during the alkaline etching process. This intrinsic thermodynamic driving force triggered the recrystallization of the CoAl(OH)$_x$ catalyst, leading to a distinct evolution from a sheet-like to a nanoparticle-like morphology.[20,21] The small-sized nanoparticles provide an effective pathway for exposing more active sites, particularly at the edges where numerous coordinated unsaturated sites are present. This enhanced exposure holds considerable potential to markedly boost the catalytic activity of reactive sites.[22] The high-resolution transmission electron microscopy (HR-TEM) image of CdS/CoAl(OH)$_x$-R displays a lattice fringe with a spacing of 0.32 nm, corresponding to the (101) crystal plane of CdS (Fig. 1g).[23] CoAl(OH)$_x$-R exhibits a morphology characterized by small nanoparticles and lacks distinct lattice fringes, which is

attributed to its low crystallinity or content. Fig. 1h–n show the high-angle annular dark-field (HAADF) image, elemental content plots, and corresponding elemental mapping images of Cd, S, Co, Al, and O in the CdS/CoAl(OH)$_x$-R catalyst.

The crystal structures of various CdS composites were examined using X-ray diffraction (XRD), as shown in Fig. 2a. Regardless of their structural differences, all CdS composites could be assigned to the hexagonal wurtzite phase (JCPDS no. 41-1049).[24] Upon loading the cocatalyst, no distinct diffraction peaks corresponding to Co(OH)$_x$ (Fig. S2) or CoAl(OH)$_x$ are observed, indicating that the catalysts obtained *via* the solvothermal method exhibit relatively low crystallinity or low loading. In the Raman spectra, two distinct peaks are located at 303 and 603 cm^{-1}, corresponding to the first-order longitudinal optical (1-LO) mode and the second-order (2-LO) mode of CdS,[25] respectively (Fig. 2b). Compared to pure CdS, the Raman peaks of the CdS/CoAl(OH)$_x$-R composite show a significant shift towards lower wavenumbers, suggesting a strong electronic interaction between CoAl(OH)$_x$-R and CdS. In contrast, the Raman peak of CdS/CoAl(OH)$_x$ and CdS/Co(OH)$_x$ does not exhibit any noticeable shift (Fig. S3). Upon heating and stirring CoAl(OH)$_x$ in an alkaline solution, Al was etched from the material. And, the elemental contents of Co and Al in the various materials were quantified using inductively coupled plasma optical emission spectrometry (ICP-OES). As depicted in Fig. 2c, prior to the alkaline etching process, the atomic ratio of Co to Al was 4.67. Upon varying the duration of alkali etching, it was observed that the Al content decreased sharply, while the Co content experienced only a minor reduction (Table. S1). The persistence of trace amounts of Al can be attributed to the dissolution equilibrium of Al^{3+} in the NaOH solution, resulting

in trace amounts of Al(OH)$_n^-$ being adsorbed onto the surface of catalyst.[21]

Fig. S4 presents the X-ray photoelectron spectroscopy (XPS) spectra of CdS/CoAl(OH)$_x$-R, CdS/CoAl(OH)$_x$, and CdS/Co(OH)$_x$, indicating the presence of Al in both CdS/CoAl(OH)$_x$-R and CdS/CoAl(OH)$_x$. Specifically, the peak at 74.1 eV in the Al 2p spectra can be attributed to the presence of the Al^{3+} oxidation state in CdS/CoAl(OH)$_x$-R and CdS/CoAl(OH)$_x$ (Fig. S5).[26] The XPS spectra of O 1s exhibited three main peaks for CdS/CoAl(OH)$_x$-R at approximately 529.7 eV, 530.6 eV, and 532.2 eV, corresponding to the metal–oxygen (M–O) bond, metal–hydroxide (M–OH) bond, and adsorbed oxygen (O$_{ads}$),[27] respectively (Fig. 2d). Remarkably, the presence of numerous M–OH bonds suggests that the primary components of both CdS/CoAl(OH)$_x$-R and CdS/CoAl(OH)$_x$ samples are metal hydroxides, with the cocatalyst being the main constituent. The CdS/Co(OH)$_x$ possess abundant M–O bonds due to the facile dehydroxylation of Co(OH)$_x$, which lacks the structural stabilization provided by hydroxyl groups, typically offered by Al^{3+}. The peak area ratio of S$_{M-O}$/S$_{M-OH}$ in CdS/CoAl(OH)$_x$-R and CdS/CoAl(OH)$_x$ indicates that alkaline etching targets the M–OH bonds in CoAl(OH)$_x$, leading to the deprotonation and dissolution of hydroxyl groups. The residual O^{2-} species from partially deprotonated –OH groups then form stable M–O bonds. Furthermore, the etching process exposes more inherent M–O bonds that were originally embedded within the CoAl(OH)$_x$ framework. Subsequently, electron paramagnetic resonance (EPR) spectroscopy was employed to characterize the CdS/CoAl(OH)$_x$ and CdS/CoAl(OH)$_x$-R. No characteristic EPR signal arising from vacancies was observed in either sample (Fig. S6).

We conducted photocatalytic experiments using furfuryl alcohol (FFA) as a model substrate under visible light irradiation from a 300 W Xe lamp in an argon atmosphere. First, the catalyst quality and alkali etching time were optimized. The FFA conversion rate increased with the alkali etching time, reaching an optimal value at approximately 30 min (Fig. S7a). However, when the alkali etching time was extended to 40 min, the FFA conversion rate decreased, likely due to the slight dissolution of the CdS surface. Then, the catalyst quantity was adjusted to achieve the highest reaction efficiency. An optimal photocatalyst amount of 20 mg was established for the subsequent experiments (Fig. S7b). A variety of catalytic products of furfuryl alcohol, generated from different catalysts, were detected using high-performance liquid chromatography (HPLC). It is evident that CdS/CoAl(OH)$_x$-R exhibits significantly better FFA conversion activity (3.82 mmol g$_{cat}^{-1}$ h^{-1}) and high furfurylamine (FAM) selectivity (94.78%) compared to pristine CdS (2.71 mmol g$_{cat}^{-1}$ h^{-1}) and CdS/Co(OH)$_x$ (3.02 mmol g$_{cat}^{-1}$ h^{-1}) (Fig. 3a). Notably, compared to other reported catalysts, CdS/CoAl(OH)$_x$-R demonstrates competitive FFA conversion efficiency with good selectivity to FAM (Table S5). Additionally, CdS/CoAl(OH)$_x$-R demonstrates superior photocatalytic H$_2$ evolution activity (9.4 mmol g$_{cat}^{-1}$ h^{-1}) compared to pristine CdS (2.2 mmol g$_{cat}^{-1}$ h^{-1}) and CdS/Co(OH)$_x$ (6.8 mmol g$_{cat}^{-1}$ h^{-1}) (Fig. S8). These results suggest the important role of CoAl(OH)$_x$ on the CdS surface and the process of alkali etching. Notably, after extending the reaction time of CdS/CoAl(OH)$_x$-R to 12 h, the
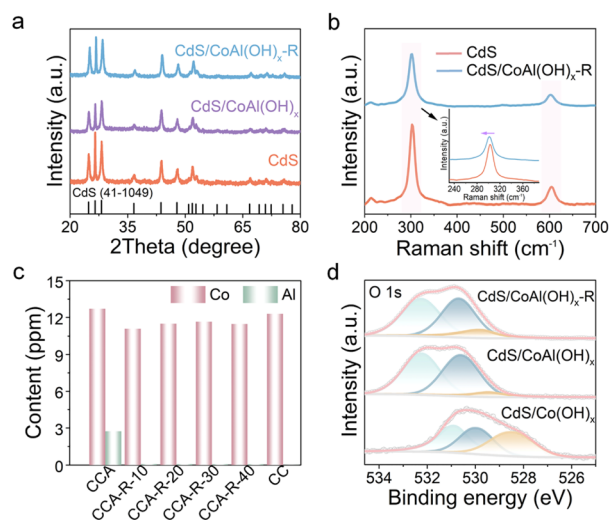

Fig. 2 (a) XRD patterns of the as-prepared samples, (b) Raman spectra of CdS and CdS/CoAl(OH)$_x$-R, (c) ICP-OES results of elements in CdS/CoAl(OH)$_x$-R with different alkali etching time. CCA: CdS/CoAl(OH)$_x$, CCA-R-10: CdS/CoAl(OH)$_x$-R-10 min, CCA-R-20: CdS/CoAl(OH)$_x$-R-20 min, CCA-R-30: CdS/CoAl(OH)$_x$-R-30 min, CCA-R-40: CdS/CoAl(OH)$_x$-R-40 min, and CC: CdS/Co(OH)$_x$, (d) high resolution XPS spectra of O 1s.
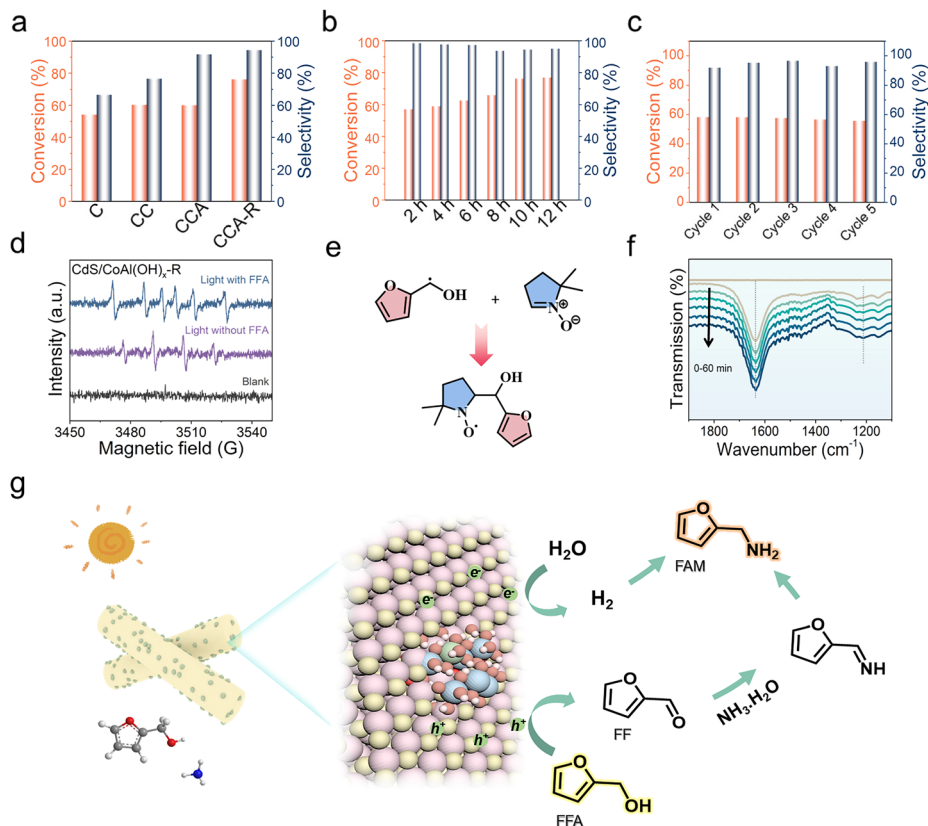
Fig. 3 Conversion rate of furfuryl alcohol and selectivity of furfurylamine (a) among different catalysts (C: CdS, CC: CdS/Co(OH)$_x$, CCA: CdS/CoAl(OH)$_x$, CCA-R: CdS/CoAl(OH)$_x$-R), (b) across various reaction times of the CdS/CoAl(OH)$_x$-R catalyst, and (c) in photocatalytic cycle experiments with CdS/CoAl(OH)$_x$-R. (d) EPR spectra of CdS/CoAl(OH)$_x$-R using DMPO as a spin trap under light irradiation, (e) spin trapping reaction of the carbon-centered radical with DMPO, (f) *in situ* FT-IR spectra in the initial stage and after 60 min for the photocatalytic process; (g) schematic mechanism of the CdS/CoAl(OH)$_x$-R for photocatalytic H$_2$ evolution coupled with FFA selective oxidation to FAM.

conversion of FFA exceeds 76.85%, and the selectivity of FAM remains at a high level (Fig. 3b). To assess the stability of CdS/CoAl(OH)$_x$-R, five consecutive photocatalytic reactions were carried out over a total of 25 h (Fig. 3c). CdS/CoAl(OH)$_x$-R retains approximately 95.61% of its initial activity. Furthermore, TEM was carried out to examine the structure and morphology of CdS/CoAl(OH)$_x$-R after photocatalysis (Fig. S9). No apparent change in the structure was observed, demonstrating that the introduction of CoAl(OH)$_x$-R can effectively inhibit the photocorrosion of CdS. Control experiments revealed that neither light irradiation alone nor the catalyst in the absence of light yielded any detectable products, thus underscoring the indispensable synergistic effect between the photocatalyst and light (Fig. S10). All the above achievements have motivated us to investigate the underlying mechanisms accounting for the enhanced catalytic activity of CdS/CoAl(OH)$_x$-R.

The electron–hole transfer was induced by two half-reactions during the photocatalytic reaction process. One involved the reduction of H$_2$O to H$_2$ through electrons, while the other was the oxidation of FFA to FF mediated by holes. Additionally, the occurrence of C–N coupling reactions typically involves the participation of free radicals. Thus, electron paramagnetic resonance (EPR) spectroscopy was employed to further identify the radical intermediates, using 5,5-dimethyl-1-pyrroline *N*-

oxide (DMPO) as a trapping agent. As illustrated in Fig. 3d and S11, under illumination, the presence of hydroxyl radicals (·OH) was detected for CdS/CoAl(OH)$_x$-R in the absence of FFA. Upon the addition of FFA, the EPR spectra exhibited six characteristic signal peaks corresponding to DMPO-·Cα radical adducts. The DMPO adduct was further analyzed using high-resolution mass spectrometry (HR-MS). The major mass peak observed at $m/z = 211.18$ was attributed to DMPO-C$_5$H$_5$O$_2$ ($m + 1$ = 211.18) (Fig. S12), confirming the formation of carbon-centered radicals derived from FFA. Therefore, C$_5$H$_5$O$_2$ is an important reaction intermediate in our system (Fig. 3e). To validate the C–N coupling mechanism, *in situ* diffuse reflection Fourier transform infrared spectroscopy (DRIFTS) experiments were conducted to further investigate the photocatalytic mechanism. As depicted in Fig. 3f, the peaks at 1635 cm^{-1} are attributed to the C=O stretching vibrations, indicating the progressive oxidation of FFA into FF.[12] Simultaneously, two IR bands at 1550 and 1150 cm^{-1} were ascribed to the δ(NH$_2$) and ν(C–N) in FAM.[28] In particular, as the photocatalytic reaction progresses, the IR band at 1580 cm^{-1}, which corresponds to the δ(N–H) bond in imines, gradually increases over time, indicating the FF undergoes reaction with NH$_3 \cdot$H$_2$O to form the imine intermediates.[29] The results suggest that the imine was further hydrogenated to FAM through hydrogen transfer.

Capture agent experiments were also conducted to identify the active species and understand the reaction process within the system. Well-known radical scavengers were employed, including triethanolamine (TEA) for photogenerated holes (h^+), silver nitrate ($AgNO_3$) for photoexcited electrons (e^-), tertiary butanol (TBA) and butylated hydroxytoluene (BHT) for hydroxyl radicals ($\cdot OH$) and carbon-centered radicals ($\cdot C$), respectively. Each scavenger was used at a concentration of 1 mmol. As shown in Fig. S13, the introduction of TEA led to a significant decrease in the conversion of FFA. This is attributed to the competitive oxidation of TEA with FFA for photogenerated holes. In contrast, the addition of $AgNO_3$ promotes the conversion of FFA. Meanwhile, the incorporation of BHT and TBA has minimal impact on the conversion of FFA. And, BHT was found to effectively inhibit the formation of FAM. Collectively, these experiments suggest that the synthesis of FAM from FFA primarily involves a dehydrogenation process of FFA to furfural.

To investigate the differences in molecular selectivity of different catalysts during photocatalysis, we examined the variations in the electronic structures of various catalysts using X-ray photoelectron spectroscopy (XPS). As depicted in Fig. 4a, the Co $2p_{3/2}$ peaks at 780.1 eV and 781.5 eV correspond to Co^{3+} and Co^{2+}, respectively.[30] The $CdS/Co(OH)_x$ sample exhibits a notably higher content of Co^{3+}, with a Co^{3+}/Co^{2+} ratio of 0.90, compared to $CdS/CoAl(OH)_x$-R, which has a Co^{3+}/Co^{2+} ratio of 0.40. This increase of Co^{2+} is attributed to the alkali etching process. A higher concentration of Co^{2+} is beneficial for the extraction of holes in the photocatalytic system, as further demonstrated in the subsequent electrochemical measurements. The electrochemical behaviors of the related samples were evaluated in 1 M KOH solution. The CV curves reveal the oxidation behavior of cobalt ions within the materials (Fig. 4b). Clearly, the characteristic peaks observed at 1.1 V and 1.4 V (vs. RHE) in $CdS/CoAl(OH)_x$-R can be attributed to the oxidation processes of $Co^{2+} \rightarrow Co^{3+}$ and $Co^{3+} \rightarrow Co^{4+}$, respectively.[30] In contrast, $CdS/Co(OH)_x$ exhibits the weak oxidation peak of Co^{3+}

$\rightarrow Co^{4+}$, while the $Co^{2+} \rightarrow Co^{3+}$ oxidation peak is difficult to observe. These findings confirm that $CdS/CoAl(OH)_x$-R generates lower-valence cobalt ions, which effectively extract photogenerated holes, thereby facilitating the occurrence of photocatalytic reactions. The combined results of the photocatalysis experiment indicate that the valence state of cobalt ions plays a crucial role in the photocatalytic reaction that converts furfuryl alcohol to furfurylamine. Furthermore, the high-resolution XPS spectra of $CdS/CoAl(OH)_x$-R and CdS (Fig. 4c and d) reveal noticeable negative shifts in the binding energies of S 2p and Cd 3d of $CdS/CoAl(OH)_x$-R. These shifts provide clear evidence of a strong electronic interaction between CdS and $CoAl(OH)_x$-R, suggesting enhanced charge transfer and interfacial coupling within the composite material. Based on the above conclusions and early reports,[8,9,31] we present the possible mechanism of FAM formation in the photocatalytic process (Fig. 3g and S14). Under irradiation, the photogenerated electrons and holes are effectively separated. The accumulated electrons drive the production of H_2, while the holes promote the oxidation of furfuryl alcohol to furfural. Subsequently, the resulting furfural reacts with ammonia water to form an imine intermediate, which then combines with the surface-generated H_2 to afford the final product, furfurylamine.

Heterogeneous photocatalytic reactions encompass several stages: the adsorption of reactant molecules, the generation and transfer of photoinduced holes/electrons, the formation of active species, catalytic reactions on the catalyst surface, and the desorption of products. These individual steps synergistically contribute to the overall performance of the photocatalytic reaction. First, a series of physical characterization studies were systematically performed. Ultraviolet-visible diffuse reflectance spectroscopy (UV/vis-DRS) was used to evaluate the light absorption ability. As shown in Fig. S15, $CdS/CoAl(OH)_x$-R demonstrated significantly enhanced absorption edges compared to both pure CdS (540 nm)[32] and $CdS/Co(OH)_x$. Additionally, the varying alkaline etching times for $CdS/CoAl(OH)_x$-R correspond to different light absorption abilities (Fig. S16). This thus implies that light absorption influences photocatalytic performance to a certain extent. The specific surface area of the catalyst was analyzed using N_2 adsorption–desorption isotherms. As shown in Fig. S17 and detailed in Table. S2, the specific surface areas of $CdS/CoAl(OH)_x$-R and $CdS/CoAl(OH)_x$ were determined to be 42.5 and 34.9 m^2 g^{-1}, respectively. This indicates that the nanoparticle structure of the alkaline etching sample possesses the larger specific surface area, thereby increasing the interface area for catalysis and enhancing its suitability for both the hydrogen evolution reaction (HER) and FFA conversion. Electrochemical active surface area (ECSA) measurements were conducted using cyclic voltammetry at various scan rates, including 20, 40, 60, 80, and 100 mV s^{-1} (Fig. S18). The calculated ECSA values are 8.00 μF cm^{-2} for $CdS/CoAl(OH)_x$ and 8.85 μF cm^{-2} for $CdS/CoAl(OH)_x$-R, respectively (Fig. S19). The higher activity area observed for $CdS/CoAl(OH)_x$-R aligns with the results of the nitrogen adsorption curve. The zeta potentials of various material surfaces were measured (Fig. S20), revealing that the composite $CdS/CoAl(OH)_x$-R possesses the highest zeta potential value,
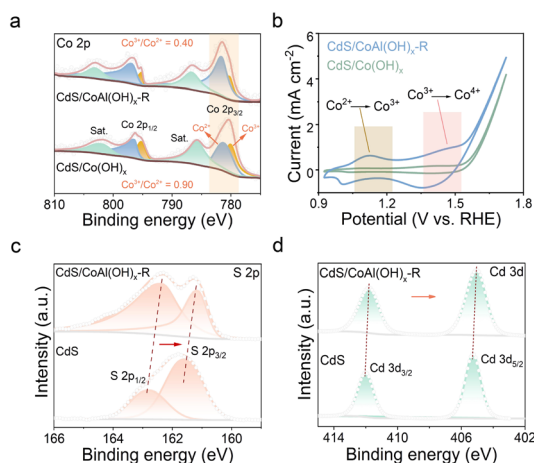

Fig. 4 High-resolution XPS spectra of (a) Co 2p, (b) CV curves for CdS, $CdS/Co(OH)_x$, and $CdS/CoAl(OH)_x$-R, and (c) high-resolution XPS spectra of S 2p and (d) Cd 3d.

indicating its enhanced capacity to adsorb furfuryl alcohol molecules at catalytic sites for the reaction.

To investigate the transfer and recombination of photogenerated charges, the photoelectrochemical properties were tested. As depicted in Fig. 5a, the photocurrent density of CdS/CoAl(OH)$_x$-R composite was significantly higher than that of CdS/Co(OH)$_x$ and CdS. Additionally, electrochemical impedance spectroscopy (EIS) revealed that the semicircle diameter of CdS/CoAl(OH)$_x$-R is smaller than that of CdS/Co(OH)$_x$ and CdS, suggesting a lower interfacial charge transfer resistance (Fig. 5b). The open circuit potential (OCP) spectrum, captured after the light is extinguished (Fig. 5c), simulates the recombination behavior of photogenerated carriers in a photocatalyst without an external applied bias. The recombination rate constant (K_r) for CdS/CoAl(OH)$_x$-R is 0.02036 s^{-1}, indicating significantly slower OCP decay kinetics compared to CdS/Co(OH)$_x$ (0.02913 s^{-1}) and CdS (0.10889 s^{-1}). In addition, the charge carrier concentration (N_d) can be determined from the slope of the Mott–Schottky (MS) plot. The N_d value for CdS/Co(OH)$_x$ is approximately 3.60×10^{17} cm^{-3}, representing an increase of about 1.9 times over that of pure CdS (1.91×10^{17} cm^{-3}). Following alkaline etching, the N_d value for CdS/CoAl(OH)$_x$-R increased to 3.73×10^{17} cm^{-3} (Fig. 5d). Photoluminescence (PL) is often used to reflect the recombination of photogenerated carriers. As shown in Fig. 5e, the primary PL emission peaks were located at ~533 nm for all samples, attributed to the recombination of electrons at the conduction band (CB) and holes at the valence band (VB).[33] Other PL peaks observed at ~565 nm can be ascribed to the recombination of electrons at CB and holes at the trap-state. CdS/CoAl(OH)$_x$-R exhibits the lowest intensity, suggesting the suppressed recombination of photogenerated carriers. Additionally, time-

resolved photoluminescence (TRPL) spectra were measured with the excitation wavelength set to 530 nm (Fig. 5f and Table S3). The decay curves of the prepared samples fit well with a double-exponential equation.[34] The average lifetime (τ_{avg}) of CdS/CoAl(OH)$_x$-R (2.27 ns) is significantly longer than that of CdS (0.53 ns) and CdS/Co(OH)$_x$ (1.08 ns), indicating a higher photogenerated carrier separation efficiency.

To further explore charge transfer kinetics at complex material interfaces, intensity-modulated photocurrent spectroscopy (IMPS) and scanning photoelectrochemical microscopy (SPECM) were utilized. These techniques provide quantitative information to understand the carrier kinetics processes involved in photocatalysis. IMPS is a frequency-domain technique used to measure the phase shift of the photocurrent response relative to the sinusoidally modulated incident light intensity.[35] By combining transient photocurrent spectra with IMPS data, the charge transfer rate (K_{ct}) and the recombination rate (K_{re}) at the sample interface can be determined (Fig. 6a and b). As depicted in Fig. S21, the photocurrent of both CdS and CdS/Co(OH)$_x$ samples exhibited a rapid decrease, indicating severe electron and hole recombination. In contrast, the transient photocurrent of the CdS/CoAl(OH)$_x$-R sample decreased more slowly. From Fig. 6c, it is evident that the K_{re} value exceeds that of K_{ct} for pure CdS, indicating that surface recombination behavior is predominant in the charge transfer process. The incorporation of Co(OH)$_x$ significantly enhances the charge transfer rate and diminishes the surface recombination rate. As previously documented,[36] the frequency corresponding to the smallest imaginary component is directly proportional to the transient time (τ_d) value. τ_d can be calculated using the formula $\tau_d = (2\pi f_{min})^{-1}$. The τ_d value of CdS/CoAl(OH)$_x$ (0.36 ms) decreased in comparison to that of pure CdS (0.44 ms), as illustrated in Fig. 6d. Notably, alkali-etched CdS/
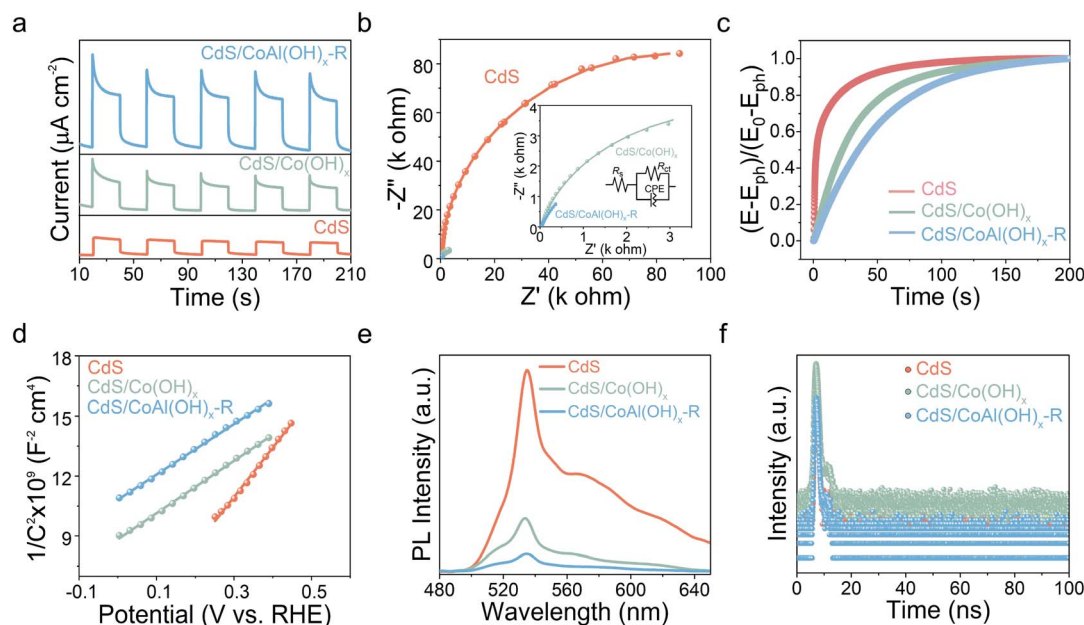

Fig. 5 (a) Transient photocurrent response, (b) EIS curves, (c) open-circuit potential decay curves, (d) M−S curves, (e) PL spectra, (f) TRPL spectra of CdS, CdS/Co(OH)$_x$ and CdS/CoAl(OH)$_x$-R.
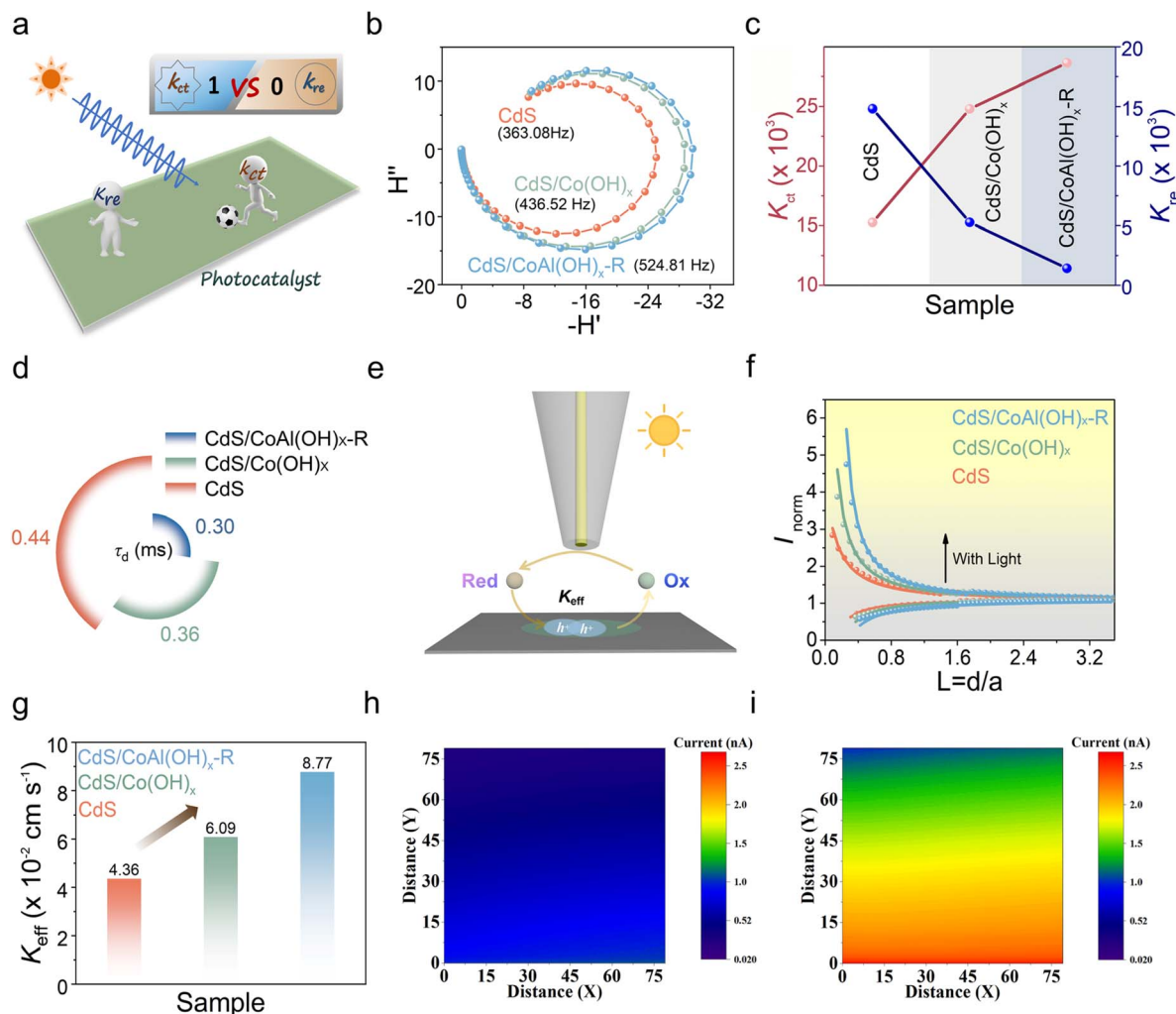
Fig. 6 (a) Principle of the IMPS setup, (b) IMPS curves, (c) K_{re} and K_{ct} values of CdS, CdS/Co(OH)$_x$ and CdS/CoAl(OH)$_x$-R, (d) τ_d values, (e) principle of the SPECM setup, (f) probe approach curves, (g) K_{eff} of CdS, CdS/Co(OH)$_x$ and CdS/CoAl(OH)$_x$-R, (h) and (i) SPECM images of the CdS/CoAl(OH)$_x$-R surface under dark and light conditions.

CoAl(OH)$_x$ (CdS/CoAl(OH)$_x$-R) can further inhibit the surface recombination of charges, as evidenced by a τ_d value of 0.30 ms.

To further elucidate the specific state of charge transfer at the interface of different materials, the charge transfer rate constant was quantitatively measured using SPECM. SPECM records the redox current generated by the ultra-microelectrode (UME) (Fig. S22) in the presence of probe molecules K$_3$[Fe(CN)$_6$] using the feedback mode (Fig. 6e). According to the previously established theoretical model,[37] the hole transfer rate constant (K_{eff}) of CdS/CoAl(OH)$_x$-R (8.77×10^{-2} cm s^{-1}) was significantly higher than those of CdS (4.36×10^{-2} cm s^{-1}) and CdS/Co(OH)$_x$ (6.09×10^{-2} cm s^{-1}) (Fig. 6f and g). The above results verify that CdS/CoAl(OH)$_x$-R can effectively promote electron–hole pair separation and expedite charge migration across the interfaces, further resulting in improved efficiency for photocatalytic hydrogen production and the conversion of furfuryl alcohol species. Subsequently, the SPECM morphology of CdS/CoAl(OH)$_x$-R was measured in constant height under dark and illumination conditions. As depicted in Fig. 6h and i, the current density was relatively low in the dark, exhibiting a distinct cold tone. Upon

irradiation, the surface produced more warm tones, indicating a higher current density. These findings suggest that a greater number of photogenerated holes accumulate on the surface and are involved in the photocatalytic reaction.

Conclusions

In summary, we reported a novel strategy for catalyst reconstruction aimed at enhancing the photocatalytic conversion of biomass molecules into clean energy and high-value products. Utilizing CdS/CoAl(OH)$_x$ as the template, it was etched in an alkaline solution, resulting in CdS/CoAl(OH)$_x$-R with morphological and electronic state transformations. The experimental findings suggest that the reconstructed catalyst features a tight charge transfer interface and numerous active sites. The charge transfer rate at the CdS/CoAl(OH)$_x$-R interface is twice that of pure CdS. The photocatalytic experiments demonstrated that CdS/CoAl(OH)$_x$-R achieved a conversion rate of 76.32% for FFA and a selectivity of 94.78% for FAM.

Author contributions

Conflicts of interest

There are no conflicts to declare.

Data availability

The data supporting this article have been included as part of the supplementary information (SI). Supplementary information: preparation methods, material characterization, photocatalytic experiments, calculation methods of selectivity and conversion, free radical test, photoelectrochemical measurements, SPECM measurement, supplementary diagrams (TEM, XRD, Raman, XPS, EPR, HR-MS, DRS, BET, zeta potential, *etc.*) and tables. See DOI: https://doi.org/10.1039/d5sc08128a.

Acknowledgements

References

1 M. Xu, X. Ruan, M. Z. Shahid, D. Meng, G. Fang, C. Ding, W. Zhang, J. Leng, S. Wang, S. K. Ravi and X. Cui, *Adv. Sci.*, 2025, **12**, 2413069.

2 X. Ruan, S. Zhao, M. Xu, D. Jiao, J. Leng, G. Fang, D. Meng, Z. Jiang, S. Jin, X. Cui and S. K. Ravi, *Adv. Energy Mater.*, 2024, **14**, 2401744.

3 M. Xu, X. Ruan, D. Meng, G. Fang, D. Jiao, S. Zhao, Z. Liu, Z. Jiang, K. Ba, T. Xie, W. Zhang, J. Leng, S. Jin, S. K. Ravi and X. Cui, *Adv. Funct. Mater.*, 2024, **34**, 2402330.

4 Y. Yuan, J. Pan, W. Yin, H. Yu, F. Wang, W. Hu, L. Wang and D. Yan, *Chin. Chem. Lett.*, 2024, **35**, 108724.

5 N. Xi, E. C. dos Santos, X. Zhao, C. Cui, M. Lill, H. Lundberg, Y. Sang, H. Liu and X. Yu, *Nano Energy*, 2025, **136**, 110750.

6 Y. Zhao, X. Wu, H. Wang, M. Ma, J. Tian and X. Wang, *Nano Lett.*, 2024, **24**, 16175–16183.

7 Y. Wang, R. Zhao, Y. Xu, B. Sun, Z. Zhou, P. Yu, Y. Qu and Y. Liu, *Nano Energy*, 2025, **141**, 111103.

8 Z. Gao, L. Cai, H. Ma, Y. Zhao, H. Wu, H. Liu, Q. Wang, D. Li and J. Feng, *ACS Catal.*, 2023, **13**, 12835–12847.

9 Z. Wang, Y. Zheng, J. Feng, W. Zhang and Q. Gao, *Chem.–Eur. J.*, 2023, **29**, e202300947.

10 H. Gong, L. Wei, Q. Li, J. Zhang, F. Wang, J. Ren and X.-L. Shi, *Langmuir*, 2024, **40**, 8950–8960.

11 Y. Wei, H. Wang, Y. Qin, Y. Hu, J. Lin, S. Wan and S. Wang, *Chem. Eng. J.*, 2024, **491**, 151954.

12 B. Liu, Y. Li, Y. Guo, Y. Tang, C. Wang, Y. Sun, X. Tan, Z. Hu and T. Yu, *ACS Nano*, 2024, **18**, 17939–17949.

13 L. Chen, Z. Liu, D. Kong, Q. Tang, L.-L. Tan, Z.-M. Liang, Y. Chen, C.-X. Chen and S. Ma, *ACS Catal.*, 2025, **15**, 4858–4869.

14 P. Zhou, Q. Zhang, Z. Xu, Q. Shang, L. Wang, Y. Chao, Y. Li, H. Chen, F. Lv, Q. Zhang, L. Gu and S. Guo, *Adv. Mater.*, 2020, **32**, 1904249.

15 C.-X. Liu, K. Liu, Y. Xu, Z. Wang, Y. Weng, F. Liu and Y. Chen, *Angew. Chem., Int. Ed.*, 2024, **63**, e202401255.

16 Y. Ming, Z. Cheng, S. Shi, J. Su, W.-F. Io, H. Wu, J. Li and B. Fei, *Small*, 2024, **20**, 2309750.

17 S. Zhao, D. Pan, Q. Liang, M. Zhou, C. Yao, S. Xu and Z. Li, *J. Phys. Chem. C*, 2021, **125**, 10207–10218.

18 X. Deng, C. Liu, X. Yan, J. Fan, Q. Liang and Z. Li, *Chin. Chem. Lett.*, 2024, **35**, 108942.

19 P. Bai, J. Lang, Y. Wang, H. Tong, Z. Wang, B. Zhang, Y. Su and Z. Chai, *Renewable Energy*, 2024, **226**, 120484.

20 W. Liu, J. Yu, T. Li, S. Li, B. Ding, X. Guo, A. Cao, Q. Sha, D. Zhou, Y. Kuang and X. Sun, *Nat. Commun.*, 2024, **15**, 4712.

21 Q. Xie, Z. Cai, P. Li, D. Zhou, Y. Bi, X. Xiong, E. Hu, Y. Li, Y. Kuang and X. Sun, *Nano Res.*, 2018, **11**, 4524–4534.

22 Y. Wang, M. Qiao, Y. Li and S. Wang, *Small*, 2018, **14**, 1800136.

23 J. Tao, M. Wang, X. Zhang, L. Lu, H. Tang, Q. Liu, S. Lei, G. Qiao and G. Liu, *Appl. Catal., B*, 2023, **320**, 122004.

24 Y. Tang, F. Ye, B. Li, T. Yang, F. Yang, J. Qu, X. Yang, Y. Cai and J. Hu, *Small*, 2024, **20**, 2400376.

25 F. Liu, Z. Wang, Y. Weng, R. Shi, W. Ma and Y. Chen, *ChemCatChem*, 2021, **13**, 1355–1361.

26 G. Xu, S.-J. Dong, H.-J. Liu, W.-B. Wang, X.-M. Zhang, M.-Q. Cai, J. Sun and J.-L. Song, *Small*, 2025, **21**, 2409455.

27 L. Zhang, B. Wang, W. Yang, L. Ju, Z. Fu, L. Zhao, Y. Jiang, H. Wang, X. Wang and C. Lyu, *Chin. Chem. Lett.*, 2025, 111142.

28 Z. Xue, S. Wu, Y. Fu, L. Luo, M. Li, Z. Li, M. Shao, L. Zheng, M. Xu and H. Duan, *J. Energy Chem.*, 2023, **76**, 239–248.

29 H. Wang, P. Hu, J. Zhou, M. B. J. Roeffaers, B. Weng, Y. Wang and H. Ji, *J. Mater. Chem. A*, 2021, **9**, 19984–19993.

30 P. Zhou, X. Lv, H. Huang, B. Cheng, H. Zhan, Y. Lu, T. Frauenheim, S. Wang and Y. Zou, *Adv. Mater.*, 2024, **36**, 2312402.

31 J. Di, Q. Li, C. Ma and Y.-C. He, *Bioresour. Technol.*, 2023, **369**, 128425.

32 B. Qiu, L. Cai, N. Zhang, X. Tao and Y. Chai, *Adv. Sci.*, 2020, **7**, 1903568.

33 B. He, C. Bie, X. Fei, B. Cheng, J. Yu, W. Ho, A. A. Al-Ghamdi and S. Wageh, *Appl. Catal., B*, 2021, **288**, 119994.

34 R. Zhang, S. Zhang, H. Xiao, J. An, Z. Wang, W. Luo, Y. Feng, B. Lu, P. Du and X. Lu, *J. Colloid Interface Sci.*, 2025, **687**, 531–539.

35 L. M. Peter, E. A. Ponomarev and D. J. Fermín, *J. Electroanal. Chem.*, 1997, **427**, 79–96.

36 Y. He, R. Zhang, Z. Wang, H. Ye, H. Zhao, B. Lu, P. Du and X. Lu, *Anal. Chem.*, 2024, **96**, 110–116.

37 S. Zhang, P. Du, H. Xiao, Z. Wang, R. Zhang, W. Luo, J. An, Y. Gao and B. Lu, *Angew. Chem., Int. Ed.*, 2024, **63**, e202315763.